IOP Publishing Plasma Physics and Controlled Fusion
Plasma Phys. Control. Fusion **65** (2023) 075005 (9pp) https://doi.org/10.1088/1361-6587/accd1d

The performance of equilibrium radial electric field shear on microturbulence with different magnetic shears in tokamak plasmas

Y C Chen[1], Y Q Qin[1], G Y Sun[1,*] and Z Lin[2]

[1] Department of physics, Xiamen University, Xiamen 361000, People's Republic of China
[2] Department of Physics and Astronomy, University of California, Irvine, CA 92697, United States of America

E-mail: gysun@xmu.edu.cn

Received 1 February 2023, revised 28 March 2023
Accepted for publication 14 April 2023
Published 23 May 2023

Abstract

Global gyrokinetic particle simulations show that equilibrium radial electric field (E_r) shear reduces the linear growth rate, ion heat conductivity, and nonlinear turbulence amplitude for both the ion temperature gradient (ITG) and kinetic ballooning mode (KBM) microturbulence by tilting the poloidal mode structure. The increase in the magnetic shear enhances the stabilizing performance of the E_r shear on linear growth rate for the ITG case but has no effect on that for the KBM case. The radial correlation length of the ITG turbulence is decreased by increasing the magnetic shear in a weak ion diamagnetic flow shear condition with low β, leading to a reduction in the effective $E \times B$ shearing rate, which weakens the suppression performance of the E_r shear on the ITG turbulence amplitude. In contrast, under a larger ion diamagnetic shear flow for higher β, an increase in magnetic shear strengthens the suppression performance of the E_r shear on the KBM turbulence amplitude due to an increase in the effective shearing rate by increasing the radial correlation length of the turbulence.

Keywords: radial electrical field, magnetic shear, ion temperature gradient, kinetic ballooning mode, microturbulence

(Some figures may appear in colour only in the online journal)

1. Introduction

Various studies have shown that the radial electric field (E_r) shear has a stabilizing effect on microturbulence and reduces the turbulent transport level to improve the plasma confinement in burning plasma devices (Wan *et al* 2013, Taimourzadeh *et al* 2019, Fu *et al* 2021, Wang *et al* 2021). However, the effects of the E_r shear on microturbulence and transport may be influenced by other plasma characteristic quantities. Self-generated zonal flows, for instance, can decrease the correlation length of the ambient turbulence in the radial direction to weaken the E_r shear effects. It is of considerable physical interest to understand the performance of the E_r shear on microturbulence and transport for a better operational stability in fusion plasma.

The evolution of the radial electric field well has been observed near the L–H transition in the experiment, and E_r can be measured using various methods, such as an equilibrium and reconstruction fitting code (EFIT), heavy ion beam probe, Doppler backscattering and lowest order radial force balance equation (Stott 1992, Wu *et al* 2019, Silva *et al* 2021). The E_r well strongly increases with increasing injected heating power or seeding moderate radiating impurity, and its width

* Author to whom any correspondence should be addressed.

can be considered as the H-mode pedestal width (Xiao *et al* 2011, Senichenkov *et al* 2021). The E_r shear can drive a sheared plasma flow to suppress the turbulent transport at the plasma edge (Burrell *et al* 1992). It is found that the E_r shear increases the energy loss level after pedestal collapse in the Tokamak plasma (Seto *et al* 2020). Negative E_r enhanced by biasing can mitigate stochastic diffusion losses and increase the intermittency of turbulence in stellarator devices (Tykhyy and Kolesnichenko 2021, van Milligen *et al* 2022). In addition, the equilibrium radial electric field can stabilize the ion temperature gradient (ITG) instability in the field-reversed configuration (FRC) (Wang *et al* 2021). Previous studies mainly focus on the formation of E_r and its effects on turbulence and transport. The work on the performance comparison of the E_r shear in microturbulence in different plasma environments has rarely been studied yet.

In this work, the effects of the magnetic shear on the performance of the E_r shear stabilizing ITG and kinetic ballooning mode (KBM) are studied using the gyrokinetic toroidal code (GTC). Using the cyclone base case parameters, we find that the E_r shear reduces the linear growth rate for both ITG and KBM cases by tilting the poloidal mode structure. The linear growth rate, ion heat conductivity, and turbulence amplitude decrease when increasing the E_r shear. Compared with the KBM case, the suppression effects of the E_r shear on the ion heat conductivity and turbulence amplitude in the nonlinear stage for the ITG case are more significant with low E_r shear but slighter with high E_r shear. We set up three different magnetic shears to investigate the suppression performance of the E_r shear on microturbulence with different magnetic shears. The results show that the increase in magnetic shear can enhance the stabilizing performance of the E_r shear at linear growth rates for the ITG case but has no effect on that for the KBM case. Due to the different ion diamagnetic shear flows, the opposite results for the radial correlation length of the turbulence with increasing magnetic shear between ITG and KBM cases are obtained. That is, the increase in magnetic shear can reduce the radial correlation length of the turbulence for the ITG case but increase it for the KBM case, which leads to the reduction and increase in the effective $E\times B$ shearing rate for the ITG and KBM cases, respectively. This can weaken and enhance the suppression performance of the E_r shear on the nonlinear turbulence amplitude for ITG and KBM cases, respectively.

The remainder of this paper is organized as follows. The simulation model is described in section 2. The stabilizing performance of E_r shear in microturbulence with different magnetic shears is discussed in section 3. Section 4 gives a brief summary of the study.

2. Simulation model

2.1. Electromagnetic gyrokinetic equations

The collisionless gyrokinetic Vlasov equation in the five-dimensional phase space (Lee 1983) is used to describe ions:

$$\frac{\mathrm{d}}{\mathrm{d}t}f(\boldsymbol{X},\mu,v_{||},t)=\left(\frac{\partial}{\partial t}+\dot{\boldsymbol{X}}\cdot\nabla+\dot{v_{||}}\frac{\partial}{\partial v_{||}}\right)f=0, \tag{1}$$

where

$$\dot{\boldsymbol{X}}=v_{||}\frac{\boldsymbol{B}}{B_0}+\boldsymbol{v_E}+\boldsymbol{v_d}+\boldsymbol{v_{B_{||}}}, \tag{2}$$

$$v_{||}=-\frac{1}{m}\left(\frac{\boldsymbol{B^*}}{B_0}\cdot\left(\mu\nabla B_0+Z\nabla\left(\phi+\mu\delta B_{||}\right)\right)+\frac{Z}{c}\frac{\partial A_{||}}{\partial t}\right). \tag{3}$$

$\boldsymbol{X}$, μ and $v_{||}$ denote the gyrocenter position, magnetic moment and parallel velocity, respectively. Defining $\boldsymbol{b_0}\equiv\frac{\boldsymbol{B_0}}{B_0}$, $\boldsymbol{B^*}=\boldsymbol{B}+\frac{B_0 v_{||}}{\Omega}\nabla\times\boldsymbol{b_0}$ is the modified magnetic field for the motion equation, where $\Omega=\frac{ZB_0}{mc}$ is the cyclotron frequency, $\boldsymbol{B}=\boldsymbol{B_0}+\nabla\times(A_{||}\boldsymbol{b_0})$ the magnetic field, $\boldsymbol{v_E}=\frac{c\boldsymbol{b_0}\times\nabla\delta\phi}{B_0}$ the drift velocity of the perturbed electric field, $\boldsymbol{v_d}=\frac{c}{ZB_0}(mv_{||}^2\nabla\times\boldsymbol{b_0}+\mu\boldsymbol{b_0}\times\nabla B_0)$ the equilibrium magnetic drift velocity, $\boldsymbol{v_{B_{||}}}=\boldsymbol{b_0}\cdot\nabla\times\delta\boldsymbol{A}_\perp$ the drift for the perturbed parallel magnetic field.

A perturbative (δf) method (Lin *et al* 1995) has been developed in GTC to reduce the particle noise in the full-f method. In δf method, the distribution function is separated to equilibrium and perturbed parts, i.e. $f=f_0+\delta f$. Defining the propagator $\frac{\mathrm{d}}{\mathrm{d}t}\equiv L=L_0+\delta L$, then equation (1) can be written as $Lf=(L_0+\delta L)(f_0+\delta f)=0$, where

$$\begin{aligned}L_0=&\frac{\partial}{\partial t}+\left(v_{||}\frac{\boldsymbol{B}}{B_0}+\boldsymbol{v_d}\right)\cdot\nabla-\frac{1}{m}\left(\frac{\boldsymbol{B^*}}{B_0}\cdot\mu\nabla B_0\right)\frac{\partial}{m\partial v_{||}},\\ \delta L=&\left(v_{||}\frac{\nabla\times A_{||}\boldsymbol{b_0}}{B_0}+\boldsymbol{v_E}+\boldsymbol{v_{B_{||}}}\right)\cdot\nabla-\frac{1}{m}\left(\frac{\nabla\times A_{||}\boldsymbol{b_0}}{B_0}\cdot\mu\nabla B_0\right.\\ &\left.-\frac{\boldsymbol{B^*}}{B_0}Z\nabla\left(\delta\phi+\mu\delta B_{||}\right)\right)\frac{\partial}{\partial v_{||}}-\frac{\partial A_{||}}{\partial t}\frac{Z\partial}{m\partial v_{||}}.\end{aligned} \tag{4}$$

The equilibrium part f_0 is defined as $L_0 f_0=0$ and could be approximated as a shifted Maxwellian's distribution as follows: $f_0=n_0(\frac{m}{2\pi T})^{\frac{3}{2}}\exp(-\frac{m(v_{||}-v_{||0})^2+2\mu B_0}{2T})$, where $v_{||0}$ is the velocity of toroidal rotation due to parallel equilibrium flow. We define the particle weight as $w\equiv\frac{\delta f}{f}$. Then, we can obtain

$$\begin{aligned}\frac{\mathrm{d}}{\mathrm{d}t}w=&-(1-w)\left[v_{||}\frac{\nabla\times A_{||}\boldsymbol{b_0}}{B_0}\cdot\frac{\nabla f_0}{f_0}\right.\\ &-\frac{1}{mf_0}\left(\frac{\nabla\times(A_{||}\boldsymbol{b_0})}{B_0}\cdot\mu\nabla B_0-\frac{\boldsymbol{B^*}}{B_0}Z\nabla\delta\phi+\mu\delta B_{||}\right)\\ &\left.\times\frac{\partial f_0}{\partial v_{||}}-\frac{\partial A_{||}}{\partial t}\frac{Z\partial f_0}{mf_0\partial v_{||}}\right].\end{aligned} \tag{5}$$

In addition, the electrostatic potential is calculated by gyrokinetic Poisson's equation assuming a single dominant ion specie:

$$\frac{Z_i^2 n_i}{T_i}(\delta\phi-\delta\tilde{\phi})=Z_i\delta n_i-Z_i\delta n_e, \tag{6}$$

where $\delta\tilde{\phi}$ is the double gyro-averaged electrostatic potential (Lee 1983) and $\delta n_s = \int \mathrm{d}v \delta f_s$ with $\int \mathrm{d}v \equiv \frac{\pi B_0}{m_s}\int \mathrm{d}v_{||}\mathrm{d}\mu$. The gyrokinetic Ampere's law is used for obtaining the vector potential:

$$\nabla_\perp^2 A_{||} = \frac{4\pi}{c}\left(Z_e \delta n_e \mu_{||e} - Z_i \delta n_i \mu_{||i}\right). \tag{7}$$

2.2. Hybrid electron response

The perturbed part of the distribution function δf is further separated into a larger adiabatic part and a smaller non-adiabatic part for the electron response to overcome numerical difficulties due to the large electron noises in the electromagnetic gyrokinetic particle simulation incorporating simultaneously ion and electron dynamics with the realistic electron–ion mass ratio $m_\mathrm{e}/m_\mathrm{i} = 1/1837$, (Lin and Chen 2001, Holod and Lin 2013) i.e. $f_e = f_{0e} + \delta f_e = f_{0e} + \delta f_e^{(0)} + \delta h_e$ with $|\delta f_e^{(0)}| \gg |\delta h_e|$. The adiabatic part is described by

$$\frac{\delta f_e^{(0)}}{f_{0e}} = \frac{e\delta\phi_\mathrm{eff}}{T_e} - \frac{\mu}{T_e}\delta B_{||} + \left.\frac{\partial ln f_{0e}}{\partial\psi}\right|_{v_\perp}\delta\psi + \left.\frac{\partial ln f_{0e}}{\partial\alpha}\right|_{v_\perp}\delta\alpha, \tag{8}$$

where ψ and $\alpha = q(\psi)\theta - \zeta$ are equilibrium poloidal flux and magnetic field line labels respectively, with θ being the poloidal angle and ζ being the toroidal angle in magnetic coordinates. The effective potential $\delta\phi_\mathrm{eff}$ can be calculated by integrating the above equation over the velocity space with the adiabatic density response

$$\frac{e\delta\phi_\mathrm{eff}}{T_e} = \frac{\delta n_e}{n_0} + \frac{\delta B_{||}}{B_0} + \left.\frac{\partial n_0}{\partial\psi}\right|_{v_\perp}\delta\psi + \left.\frac{\partial n_0}{\partial\alpha}\right|_{v_\perp}\delta\alpha. \tag{9}$$

The non-adiabatic part is given by

$$L\delta h_e = -L(f_{0e} + \delta f_e^{(0)}) = -\delta L f_{0e} - L_0 \delta f_e^{(0)}, \tag{10}$$

and this equation can be simplified as

$$\frac{1}{f_{0e}}L\delta h_e = -\frac{\partial}{\partial t}\frac{\delta f_e^{(0)}}{f_{0e}} + \left(\frac{c\mu}{eB_0}b_0\times\nabla\delta B_{||} - v_E\right)\cdot\nabla ln f_{0e}\Big|_{v_\perp} - v_d\cdot\nabla\frac{\delta f_e^{(0)}}{f_{0e}} + \frac{e}{T_e}v_d\cdot\nabla\delta\phi - \frac{\mu}{T_e}\cdot\nabla\delta B_{||}. \tag{11}$$

2.3. Equilibrium radial electric field

Considering the effects of the equilibrium radial electric field, the electrostatic potential is extended as $\phi = \delta\phi + \phi_\mathrm{eq}$, where ϕ_eq is the equilibrium potential. Then, the operator L_0 is

$$L_0 = \frac{\partial}{\partial t} + \left(v_{||}\frac{\boldsymbol{B}}{B_0} + \boldsymbol{v_d} + \boldsymbol{v_{eq}}\right)\cdot\nabla - \frac{1}{m}\left(\frac{\boldsymbol{B^*}}{B_0}\cdot\mu\nabla B_0\right)\frac{\partial}{m\partial v_{||}}, \tag{12}$$

where the new term $v_\mathrm{eq} = \frac{cb_0\times\nabla\phi_\mathrm{eq}}{B_0}$ is the drift velocity of the equilibrium electrostatic potential. Equation (11) can now be rewritten as

$$\frac{1}{f_{0e}}L\delta h_e = -\frac{\partial}{\partial t}\frac{\delta f_e^{(0)}}{f_{0e}} + \left(\frac{c\mu}{eB_0}b_0\times\nabla\delta B_{||} - v_E\right)\cdot\nabla ln f_{0e}\Big|_{v_\perp} - (v_d + v_\mathrm{eq})\cdot\nabla\frac{\delta f_e^{(0)}}{f_{0e}} + \frac{e}{T_e}v_d\cdot\nabla\delta\phi - \frac{\mu}{T_e}\cdot\nabla\delta B_{||}. \tag{13}$$

2.4. Particle motion equations

A toroidal magnetic coordinate system (ψ,θ,ζ) is used in our simulations, where ψ,θ,ζ are poloidal magnetic flux, poloidal angle, and toroidal angle, respectively. The particle equations of motion in electromagnetic simulation using the magnetic coordinates are as follows (White and Chance 1984, Holod *et al* 2009):

$$\dot{\psi} = \frac{c}{Z}\frac{\partial\epsilon}{\partial B_0}\left(\frac{I}{D}\frac{\partial B_0}{\partial\zeta} - \frac{g}{D}\frac{\partial B_0}{\partial\theta}\right) + \frac{cI}{D}\frac{\partial\phi}{\partial\zeta} - \frac{cg}{D}\frac{\partial\phi}{\partial\theta} + v_{||}B_0\left(\frac{g}{D}\frac{\partial\lambda}{\partial\theta} - \frac{I}{D}\frac{\partial\lambda}{\partial\zeta}\right), \tag{14}$$

$$\dot{\theta} = \frac{v_{||}B_0(1-\rho_c g' - g\partial_\psi\lambda)}{D} + c\frac{g}{D}\left[\frac{1}{Z}\frac{\partial\epsilon}{\partial B_0}\frac{\partial B_0}{\partial\psi} + \frac{\partial\phi}{\partial\psi}\right], \tag{15}$$

$$\dot{\zeta} = \frac{v_{||}B_0(q + \rho_c I' + I\partial_\psi\lambda)}{D} - c\frac{I}{D}\left[\frac{1}{Z}\frac{\partial\epsilon}{\partial B_0}\frac{\partial B_0}{\partial\psi} + \frac{\partial\phi}{\partial\psi}\right], \tag{16}$$

$$\dot{\rho}_{||} = -c\frac{(1-\rho_c g') - g\partial_\psi\lambda}{D}\left[\frac{1}{Z}\frac{\partial\epsilon}{\partial B_0}\frac{\partial B_0}{\partial\theta} + \frac{\partial\phi}{\partial\theta}\right] \tag{17}$$

$$-c\frac{(q+\rho_c I') + I\partial_\psi\lambda}{D}\left[\frac{1}{Z}\frac{\partial\epsilon}{\partial B_0}\frac{\partial B_0}{\partial\zeta} + \frac{\partial\phi}{\partial\zeta}\right] \tag{18}$$

$$-c\frac{I\partial_\zeta\lambda - g\partial_\theta\lambda}{D}\left[\frac{1}{Z}\frac{\partial\epsilon}{\partial B_0}\frac{\partial B_0}{\partial\psi} + \frac{\partial\phi}{\partial\psi}\right] - \frac{\partial\lambda}{\partial t}, \tag{19}$$

where $D = gq + I + \rho_c(gI' - Ig')$ with $I' \equiv \frac{\mathrm{d}I}{\mathrm{d}\psi}$ and $g' \equiv \frac{\mathrm{d}g}{\mathrm{d}\psi}$ being radial derivatives poloidal and toroidal currents, respectively. In addition, the modified parallel canonical momentum ρ_c is given by $\rho_c = \rho_{||} + \lambda$ with $\rho_{||} = \frac{v_{||}}{\Omega} = \frac{mc}{ZB_0}v_{||}$, and $\frac{\partial\epsilon}{\partial B_0} = \mu + \frac{Z^2}{mc^2}\rho_{||}^2 B_0$ is used for short notation. These nonlinear terms are used for the motion equations in nonlinear simulations for the generation of zonal flows. The zonal field and zonal component of the electrostatic potential can be calculated by using gyrokinetic Ampére's law and Poisson equation, respectively. We found that the time-evolution of the relevant physical characteristics of the microturbulence reaches a nonlinear saturation stage after a linear growth.

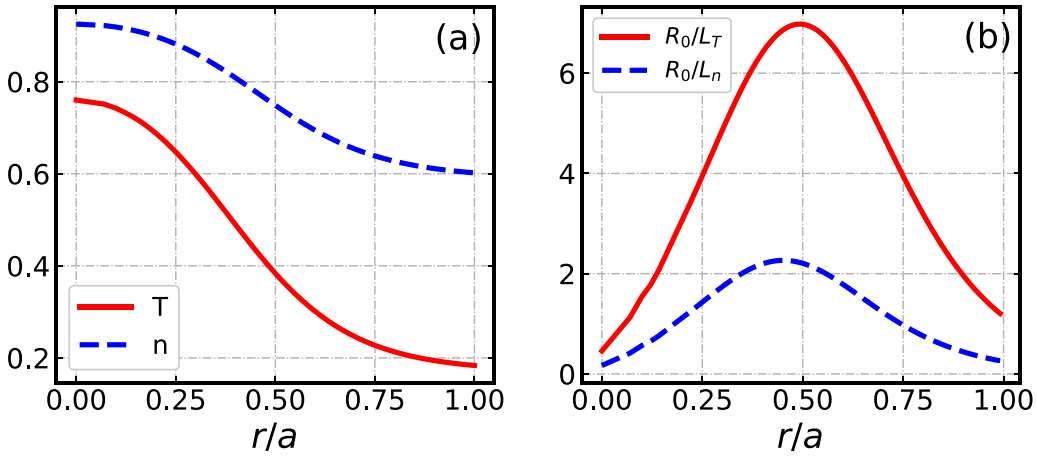

Figure 1. Panel (a) shows the radial profile of the equilibrium temperature T and density n. Panel (b) shows the radial profile of the logarithmic gradients of T and n.

2.5. Simulation parameters

The simulation parameters in this paper are as follows: the inverse aspect ratio is $a/R_0 = 0.357$, where $R_0 = 83.5$ cm is the major radius and a is the minor radius. The ion gyro-radius is $\rho_i/R_0 = 2.86 \times 10^{-3}$ with the device size $a/\rho_i = 125$. The radial profile of the safety factor in the cyclone base case (Dimits *et al* 2000, Xie *et al* 2016) is $q = 0.82 + 1.1\psi_N + 1.0\psi_N^2$, where $\psi_N = \psi/\psi_w$ is the poloidal magnetic flux normalized to the separatrix value with $\psi_w = 0.0375 B_0 {R_0}^2$. The equilibrium temperature and density are given by $T_i = T_e = 1.0 + 0.415(\tanh((0.18 - \psi_N)/0.4) - 1.0)$ and $n_i = n_e = 1.0 + 0.205(\tanh((0.30 - \psi_N)/0.4) - 1.0)$, respectively. The simulation range of the poloidal magnetic flux is $\psi = (0.02\psi_w, 0.88\psi_w)$. On the diagnostic surface, $r = 0.5a$, $q = 1.4$, $B_0 = 2$ T, $T_e = T_i = 2223$ eV, $n_e = n_i = 9 \times 10^{13}$ cm^{-3}, $R_0/L_T = 6.9$, $R_0/L_n = 2.2$, $s = \frac{rq'}{q} = 0.82$, where $L_T^{-1} = -\mathrm{d}\ln T/\mathrm{d}r$ and $L_n^{-1} = -\mathrm{d}\ln n/\mathrm{d}r$ are the characteristic lengths of temperature and density, respectively. Figure 1(a) shows the radial profile of the equilibrium temperature and density, and their logarithmic gradients are shown in figure 1(b). Based on the convergence studies, 100, 400 and 32 grid points are used in the radial, poloidal and toroidal directions, respectively. The number of particle cells is 100 for thermal ions and electrons, and the toroidal mode number n is $n = 10$. The time step size for ITG simulation is $\Delta t = 0.01 R_0/C_s$, and $\Delta t = 0.005 R_0/C_s$ for KBM cases. In addition, the homogeneous Dirichlet boundary effect is negligible due to the width of each individual harmonic of the turbulence much smaller than the radial simulation width (Li and Xiao 2017).

3. Results

3.1. Stabilizing effects of the radial electric field shear

The radial electric field shear (Taimourzadeh *et al* 2019) is given by $\omega_s = \frac{(B_p R_0)^2}{B_0} |\frac{\partial^2 \phi_{\mathrm{eq}}}{\partial \psi^2}|$, where B_p is the poloidal magnetic field. In our simulation, the radial profile of the equilibrium potential ϕ_{eq} with a constant ω_s is taken to be $\phi_{\mathrm{eq}} = \frac{\omega_s}{2B_0 {R_0}^2}(\psi - 0.02\psi_w)(0.88\psi_w - \psi)$ for arranging the radial electric field $E_\psi = -\frac{\partial \phi_{\mathrm{eq}}}{\partial \phi} = 0$ at the core of the simulation domain.

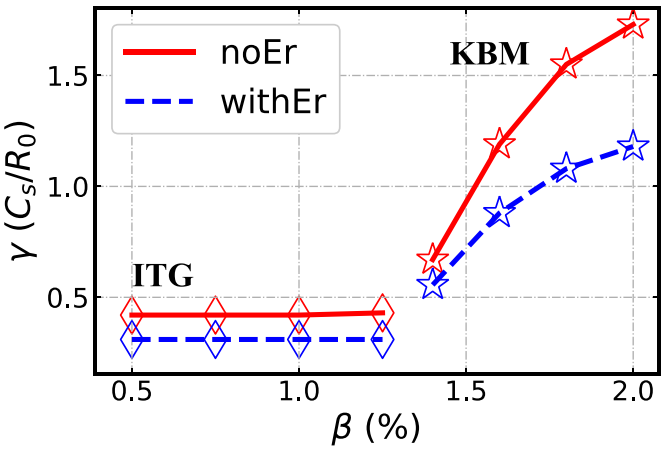

Figure 2. Growth rate γ as a function of the β_e for poloidal mode number $k_\theta \rho_i = 0.22$ on the diagnostic surface, with (blue dash) and without (red line) the radial electric field E_r. Two types of microturbulence for ITG and KBM are represented by diamond and star shapes, respectively.

Figure 2 shows a linear growth rate γ of the microinstability at $k_\theta \rho_i = 0.22$ with a β scan, where $\beta = 8\pi n T/{B_0}^2$ is the ratio between plasma and magnetic field shear and $k_\theta = nq/r$. The different β parameters are set up by varying the density. It is found that the transition from ITG to KBM appears at around $\beta = 1.3\%$ with increasing β, which is consistent with the previous results presented in Dong *et al* (2017) and Tang *et al* (2016). As β increases, the ITG growth rate is almost unchanged, while the γ of the KBM increases, which means the KBM growth compared to the ITG case is more sensitive to the β. A similar result has been reported that the KBM is very sensitive to the equilibrium implementations (Xie *et al* 2016). In addition, the growth rate is reduced when the sheared radial

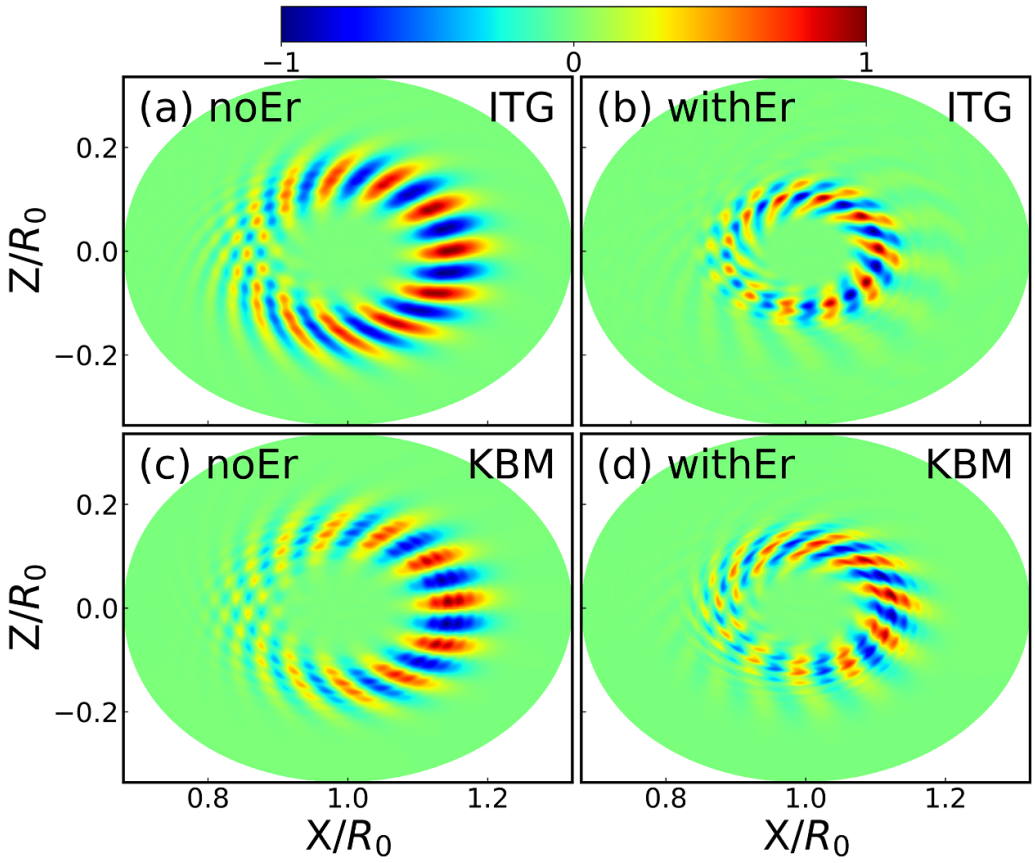

Figure 3. The two-dimensional poloidal contour of the perturbed electrostatic potential $\delta\phi$ in the linear stage, with $\beta = 1.0\%$ for ITG (upper panels) and $\beta = 2.0\%$ for KBM (lower panels), respectively. Panels (a) and (c) show the cases without radial electric field E_r, and the cases with E_r are shown in panels (b) and (d), where the E_r shear is $\omega_s = 0.5\gamma_0$. All potentials are normalized by their maximum values $\delta\phi_{\max}$.

electric field E_r is considered in simulations with $\omega_s = 0.5\gamma_0$, where γ_0 is the growth rate in the absence of the E_r shear. Note that the KBM growth rate decreases more significantly at high β compared with that at low β in the presence of the E_r shear, suggesting that the radial electric field may be an important parameter for forthcoming high-β advanced Tokamaks in microturbulence control.

Figure 3 shows that the 2D normalized poloidal contour of the perturbed electrostatic potential $\delta\phi$ for $k_\theta\rho_i = 0.22$ in the linear stage, with $\beta = 1.0\%$ for ITG and $\beta = 2.0\%$ for KBM, respectively. Left and right panels show the cases without and with radial electric field E_r ($\omega_s = 0.5\gamma_0$), respectively. In the absence of E_r, the KBM mode exhibits a distinct ballooning structure, as shown in figure 3(c), and the filament of the ITG mode seems to be smoother, as shown in figure 3(a). It is found that the E_r shear tilts the mode structure in the radial direction and reduces the radial eddy size, as shown in figures 3(b) and (d). This result is obtained because the sheared $E \times B$ flow direction is opposite in the inner ($r < 0.5a$) and outer ($r > 0.5a$) regions for a fixed ω_s in our simulations, leading to a radial variation of the local wave phase velocity. It is demonstrated that the radial tilting of the mode structure can reduce the growth rate by increasing the Landau damping (Wang *et al* 2021).

Figure 4 shows that the linear growth rate is γ, ion heat conductivity χ_i, and nonlinear turbulence amplitude $\delta\phi^2_{\rm rms}$ as a function of the normalized radial electric field shear ω_s/γ_0, with $\beta = 1.0\%$ for ITG and $\beta = 2.0\%$ for KBM, respectively. A simple power law is defined as $1 - C(\omega_s/\gamma_0)^\alpha$ to fit the curves of these quantities. The ion heat conductivity is given by $\chi_i = \frac{1}{n_i \nabla T_i}\int {\rm d}\boldsymbol{v}(\frac{1}{2}mv^2 - \frac{3}{2}T_i)v_r\delta f$, where v and v_r are the particle velocity and radial $E \times B$ drift velocity, respectively. In our simulations, both the χ_i and $\delta\phi^2_{\rm rms}$ are obtained by time-averaged over the nonlinear saturation stage. It is seen in figure 4(a) that the γ is decreased with increasing the E_r shear, and the results for the ITG and KBM are almost the same where the results can be fitted with fitting constants $C = 0.57$ and $\alpha = 0.73$ for ITG case, $C = 0.58$ and $\alpha = 0.73$ for KBM case, respectively. The dependence of the χ_i on the E_r shear is fitted with fitting constants $C = 0.96$ and $\alpha = 0.13$ for ITG case, and $C = 1.03$ and $\alpha = 0.29$ for KBM case, respectively, as shown in figure 4(b). Figure 4(c) shows the dependence of the $\delta\phi^2_{\rm rms}$ on the E_r shear, and the curves are fitted with fitting constants $C = 0.95$ and $\alpha = 0.098$ for ITG case, and $C = 1.02$ and $\alpha = 0.28$ for KBM case, respectively. Note that the fitting coefficient α is obviously larger in the KBM case for both the ion heat conductivity and nonlinear turbulence amplitude. This is because the ion pressure in the KBM case is larger due to a larger density, leading to a larger ion diamagnetic flow shear where the shear is given by $\omega_{\rm dia} = \frac{\partial\Omega_{\rm dia}}{\partial \ln R}$ with $\Omega_{\rm dia} = \frac{1}{n_i Z_i}\frac{\partial P_i}{\partial \psi}$ being the ion diamagnetic flow, which makes a slower radial tilting for the KBM case when zonal flows are

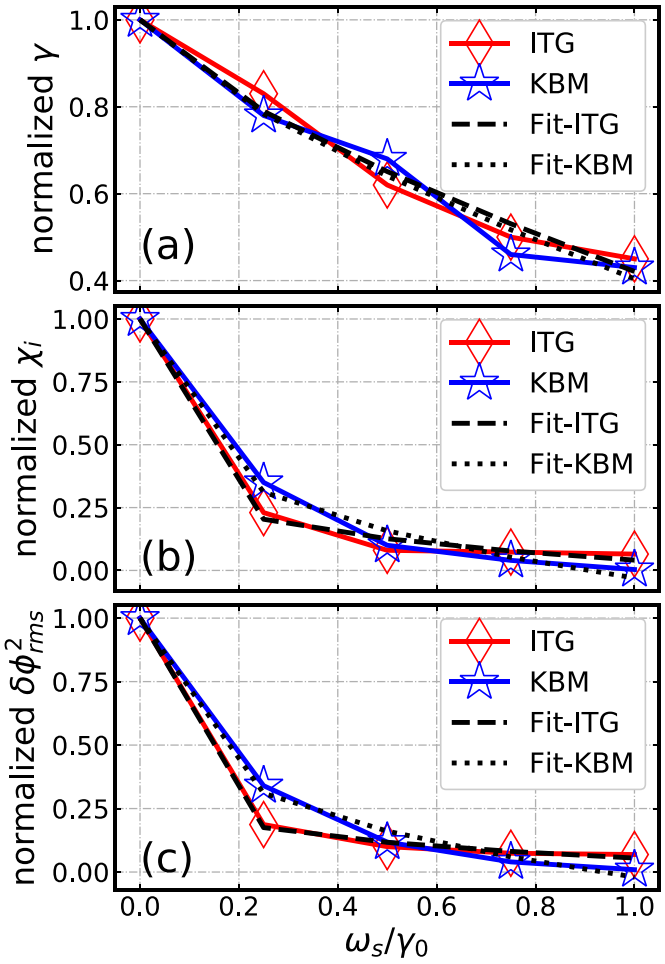

Figure 4. The linear growth rate γ (panel (a)), ion heat conductivity χ_i (panel (b)), and nonlinear turbulence amplitude $\delta\phi^2_{\rm rms}$ (panel (c)) as a function of the normalized radial electric field shear ω_s/γ_0, with $\beta = 1.0\%$ for ITG (red diamond) and $\beta = 2.0\%$ for KBM (blue star), respectively. All plotted quantities are normalized by their respective values when $\omega_s = 0$, and fitted by simple power laws (dashed and dotted lines).

generated in the nonlinear stage (see figures 7(b) and (e)). As a result, the reduction of the KBM turbulence amplitude and ion heat conductivity is slower when small E_r shear is considered, resulting in a larger α by using a power law fitting function. In addition, it is found that a remarkable similarity appears between the results of the χ_i and $\delta\phi^2_{\rm rms}$ because the ion heat transport is driven by the local fluctuation intensity where they are in phase during bursting with time evolution and their intensity satisfying a scaling of $\chi_i \propto \delta\phi^2_{\rm rms}$ (Lin *et al* 1999, Xiao and Lin 2009).

3.2. Performance of the radial electric field shear with different magnetic shear

Different magnetic shears are set up to compare the performance of the radial electric field shear on the ITG and KBM by varying the radial profile of the safety factor with the form $q = C_1 + C_2\psi_N + C_3\psi_N^2$, where $\{C_1, C_2, C_3\}$ are the adjustable parameters to control the profile details. $\{C_1, C_2, C_3\} = \{0.82, 1.1, 1.0\}$ is used for the magnetic shear $s = 0.82$ in the cyclone base case, which is described in section 2. In addition, we set $\{C_1, C_2, C_3\} = \{0.9, 1.23, 0.14\}$ for $s = 0.58$, and $\{C_1, C_2, C_3\} = \{0.76, 1.02, 1.60\}$ for $s = 0.99$, respectively. The q value satisfies $q(r = 0.5a) = 1.4$ for each profile of the safety factor to keep the most unstable mode staying at $k_\theta\rho_i = 0.22$. The radial profiles of the safety factor and their corresponding magnetic shear are shown in figures 5(a) and (b), respectively. It is found in our simulations that the linear growth rate for both ITG and KBM cases decreases with increasing magnetic shear in the absence of E_r shear, which is very consistent with the results shown in Zhao *et al* (2021). The growth rates are $\{0.43, 0.42, 0.37\}C_s/R_0$ for ITG cases, and $\{1.95, 1.73, 1.34\}C_s/R_0$ for KBM cases, corresponding to the magnetic shear $s = \{0.58, 0.82, 0.99\}$, respectively.

Figure 6 shows the linear growth rate and nonlinear turbulence amplitude versus the E_r shear with different magnetic shears for ITG and KBM cases, respectively. The suppression performance of the E_r shear on the ITG linear growth rate increases with increasing magnetic shear, as shown in figure 6(a). In contrast, the E_r shear has no effect on the KBM linear growth rate, as shown in figure 6(c). As the magnetic shear increases, the suppression performance of the E_r shear on the nonlinear turbulence amplitude decreases for ITG cases and increases for KBM cases, respectively. To explain the different results of E_r effects on turbulence and transport between ITG and KBM cases, the poloidal contour of the perturbed electrostatic potential in the absence of the E_r shear is plotted, as shown in figure 7. It is shown in figures 7(a)–(c) that the radial eddy size of the turbulence is reduced by increasing the magnetic shear for ITG cases. In contrast, the radial eddy size is increased by increasing the magnetic shear for KBM cases, as shown in figures 7(d)–(f). To estimate the radial eddy size of the turbulence, the two-point correlation function defined as $C_{r\theta}(\Delta r, \Delta\theta) = \frac{\langle\delta\phi(r+\Delta r,\theta+\Delta\theta)\delta\phi(r,\theta)\rangle}{\sqrt{\langle\delta\phi^2(r+\Delta r,\theta+\Delta\theta)\rangle\langle\delta\phi^2(r,\theta)\rangle}}$ is calculated, where Δr and $\Delta\theta$ are the radial and poloidal separations, respectively. The operator $\langle\cdots\rangle$ represents the average over $\psi_N = [0.3, 0.7]$ and $\theta = [0, 2\pi]$. Then, we can get the 1-D radial correlation function $C_r(\Delta r)$ by using the maximal value along the ridge of $C_{r\theta}(\Delta r, \Delta\theta)$. The 1-D radial correlation function exhibits Gaussian decay for small separations, i.e. $C_r(\Delta r) \approx \exp[-(\Delta r/L_r)^2]$, where L_r is the radial correlation length of the turbulence, and its value is also shown in figure 7 panels. It is found that L_r decreases for ITG cases but increases for KBM cases with increasing magnetic shear, leading to a reduction and increase in the effective $E \times B$ shearing rate, respectively, where the effective shearing rate is dependent on the ratio of the correlation lengths of the ambient turbulence in the radial and toroidal directions (Hahm and Burrell 1995). This is because both the magnetic shear and ion diamagnetic flow shear have effects on the tilting mode structure but with opposite directions. The ion diamagnetic flow shear for the ITG case is weaker due to a lower plasma pressure, so its eddies are easily broken with a reduction of the radial correlation lengths when the magnetic shear increases, as shown in

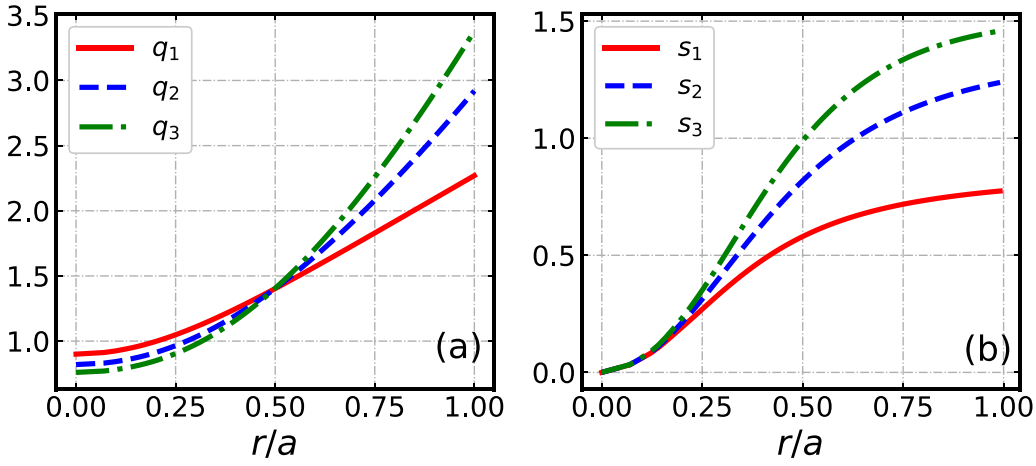

Figure 5. Panel (a) shows radial profiles of the safety factor q, where the magnetic shear s is 0.58, 0.82, and 0.99 on the diagnostic surface $r/a = 0.5$, for q_1, q_2, and q_3, respectively. Panel (b) shows the corresponding magnetic shear profiles.

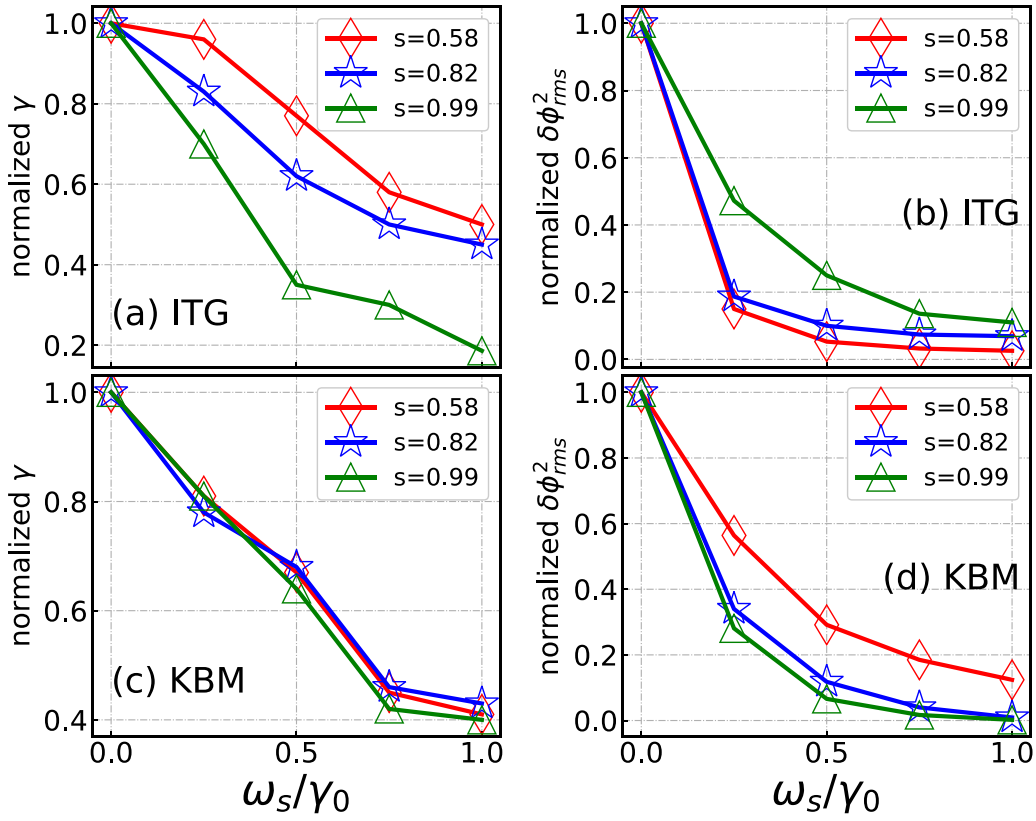

Figure 6. Panels (a) and (c) show the linear growth rate γ as a function of the E_r shear, with different magnetic shears for ITG and KBM cases, respectively. Panels (b) and (d) show the nonlinear turbulence amplitude $\delta\phi^2_{\rm rms}$ as a function of the E_r shear, with different magnetic shears for ITG and KBM cases, respectively. All plotted quantities are normalized by their respective values when $\omega_s = 0$.

figures 7(a)–(c). By comparing with figure 7(c), we can see in figure 7(d) that the KBM mode structure eddies are tilted and broken along the opposite direction with a small magnetic shear due to a larger ion diamagnetic flow shear for higher β. Therefore, the dependence of the radial correlation lengths on the magnetic shear is opposite for the ITG and KBM cases as the magnetic shear increases from 0.58 to 0.99. Hence, a feasible explanation is that the suppression performance of the E_r shear on the nonlinear turbulence amplitude is decreased for ITG cases by increasing the magnetic shear due to the reduction of the effective $E \times B$ shearing rate. In contrast, the suppression performance of the E_r shear on the nonlinear turbulence amplitude is increased for KBM cases by increasing the magnetic shear due to the increase of the effective $E \times B$ shearing rate.

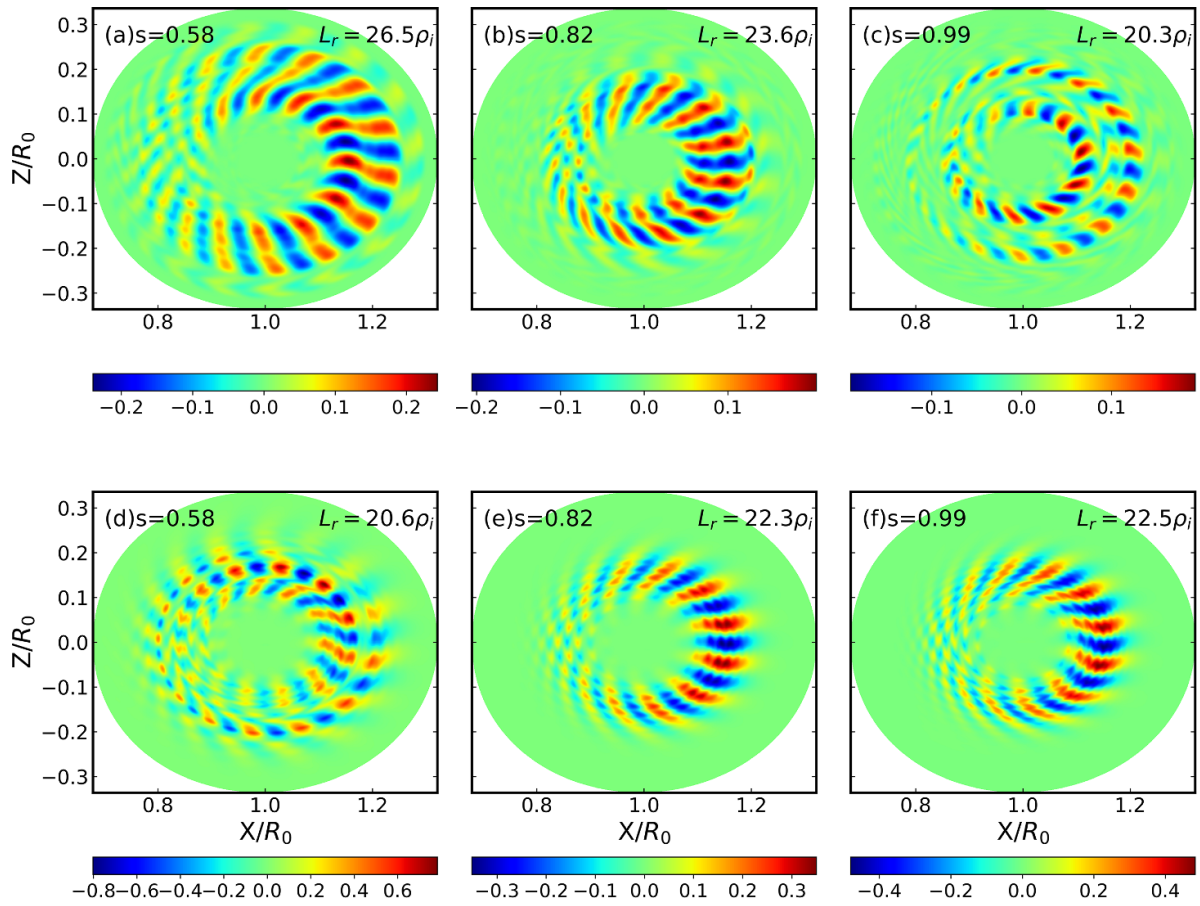

Figure 7. The two-dimensional poloidal contour of the perturbed electrostatic potential $\delta\phi$ in the nonlinear stage with different magnetic shears. Upper panels (a)–(c) show the results for the ITG cases with magnetic shear $s = 0.58$, $s = 0.82$ and $s = 0.99$, respectively. Lower panels (d)–(f) show the results for the KBM cases with magnetic shear $s = 0.58$, $s = 0.82$, and $s = 0.99$, respectively. The radial correlation length is shown in the right upper in each panel.

4. Summary

The GTC simulations show the stabilizing effects of the E_r shear on ITG and KBM micro-instabilities due to the increase in the Landau damping by tilting the poloidal mode structure. The performance of the E_r shear effect on the linear growth rate is almost the same for ITG and KBM cases using cyclone base case parameters. The performance of the E_r shear effects on ion heat conductivity and nonlinear turbulence amplitude is slightly different between ITG and KBM cases due to the different ion diamagnetic flow shears. The increase in magnetic shear can enhance the stabilizing performance of the E_r shear at the linear growth rate for the ITG case but has no effect on the KBM case. Meanwhile, the suppression performance of the E_r shear on the nonlinear turbulence amplitude is weakened with increasing the magnetic shear for the ITG case but enhanced for the KBM case, which may be because the increase in magnetic shear reduces the effective $E \times B$ shearing rate by reducing the radial correlation length of the turbulence for the ITG case with a weak ion diamagnetic shear flow. In contrast, the effective $E \times B$ shearing rate is increased by increasing the radial correlation length of the turbulence for the KBM case under a larger ion diamagnetic shear flow with higher β. This work is a first step toward a thorough understanding of the E_r shear performance of microturbulence under different plasma fusion conditions. In the future, we will improve our simulation model by considering a more comprehensive and realistic physical environment, such as fast ions and collision effects. A more experimentally realistic E_r profile will also be considered in the simulation. In addition, the exploration of the performance of the E_r shear on microturbulence will be extended to stellarator and FRC devices.

Data availability statement

The data cannot be made publicly available upon publication because they contain commercially sensitive information. The data that support the findings of this study are available upon reasonable request from the authors.

Acknowledgments

The authors would like to thank the GTC team for constructive discussions. This work was supported by the National Key R&D Program of China under Grant No. 2017YFE0301201 and the National Natural Science Foundation of China (NSFC) under Grant No. 11275162.

ORCID iDs

Y C Chen https://orcid.org/0000-0001-9054-2791
Y Q Qin https://orcid.org/0000-0003-4927-1648
G Y Sun https://orcid.org/0000-0001-6382-6254
Z Lin https://orcid.org/0000-0003-2007-8983

References

Burrell K H *et al* 1992 *Plasma Phys. Control. Fusion* **34** 1859
Dimits A M *et al* 2000 *Phys. Plasmas* **7** 969–83
Dong G, Bao J, Bhattacharjee A, Brizard A, Lin Z and Porazik P 2017 *Phys. Plasmas* **24** 081205
Fu J Y, Nicolau J H, Liu P F, Wei X S, Xiao Y and Lin Z 2021 *Phys. Plasmas* **28** 062309
Hahm T S and Burrell K H 1995 *Phys. Plasmas* **2** 1648–51
Holod I and Lin Z 2013 *Phys. Plasmas* **20** 032309
Holod I, Zhang W L, Xiao Y and Lin Z 2009 *Phys. Plasmas* **16** 122307
Lee W W 1983 *Phys. Fluids* **26** 556–62
Li Y and Xiao Y 2017 *Phys. Plasmas* **24** 081202
Lin Z and Chen L 2001 *Phys. Plasmas* **8** 1447–50
Lin Z, Hahm T S, Lee W W, Tang W M and Diamond P H 1999 *Phys. Rev. Lett.* **83** 3645–8
Lin Z, Tang W and Lee W 1995 *Phys. Plasmas* **2** 2975–88
Senichenkov I, Kaveeva E, Rozhansky V and Coster D 2021 *Phys. Plasmas* **28** 062507
Seto H, Xu X, Dudson B and Yagi M 2020 *Contrib. Plasma Phys.* **60** e201900158
Silva C *et al* 2021 *Nucl. Fusion* **61** 126006
Stott P 1992 *Nucl. Fusion* **32** 167–75
Taimourzadeh S, Shi L, Lin Z, Nazikian R, Holod I and Spong D 2019 *Nucl. Fusion* **59** 046005
Tang T F, Xu X Q, Ma C H, Bass E M, Holland C and Candy J 2016 *Phys. Plasmas* **23** 032119
Tykhyy A and Kolesnichenko Y 2021 *Plasma Phys. Control. Fusion* **63** 075019
van Milligen B P, Carreras B A, García L, Grenfell G, Voldiner I and Hidalgo C (The TJ-II Team) 2022 *Plasma Phys. Control. Fusion* **64** 055006
Wan W, Parker S E, Chen Y, Groebner R J, Yan Z, Pankin A Y and Kruger S E 2013 *Phys. Plasmas* **20** 055902
Wang W H, Bao J, Wei X S, Lin Z, Choi G J, Dettrick S, Kuley A, Lau C, Liu P F and Tajima T 2021 *Plasma Phys. Control. Fusion* **63** 065001
White R B and Chance M S 1984 *Phys. Fluids* **27** 2455–67
Wu J, Chen Y C, Chen P, Chen Y J, Yao L M and Fu J L 2019 *IEEE Trans. Plasma Sci.* **47** 457–61
Xiao X, Liu L, Zhang X and Wang S 2011 *Phys. Plasmas* **18** 032504
Xiao Y and Lin Z 2009 *Phys. Rev. Lett.* **103** 085004
Xie H S, Xiao Y, Holod I, Lin Z and Belli E A 2016 *J. Plasma Phys.* **82** 905820503
Zhao Y, Wang J, Liu D, Chen W, Dong G and Lin Z 2021 *Phys. Plasmas* **28** 012107